Newtonian and Non-Newtonian Models of the Hollow All-Polymer Bragg Fiber Drawing

Elio Pone, Charles Dubois, Ning Guo, Suzanne Lacroix, and Maksim Skorobogatiy

***Abstract*—Profile development during the isothermal drawing of the hollow all-polymer Bragg fibers is studied in the case when surface tension is strong enough to cause a hole collapse. The viscoelastic model of polymer flow is considered, and a comparison with the simpler Newtonian and generalized Newtonian models is made. The effects of draw ratio, draw temperature, feeding speed, core pressurization, and mismatch of material properties in the multilayer structure are investigated. A relation between the hole collapse and the layers nonuniformity is presented, and their effect on the fiber-transmission properties is investigated.**

***Index Terms*—Bragg reflectors, fiber design and fabrication, fiber materials, multilayers, polymers.**

I. Introduction

THE MOTIVATION for this paper is the fabrication of hollow multilayered polymer optical fibers. Such fibers have been demonstrated to guide electromagnetic radiation in a wide range of frequencies from the visible to terahertz. Hollow core fibers promise a considerable advantage over their solid core counterparts in applications related to high-power guidance for military, industry, and medicine, as well as infrared imaging and sensing [1]–[7]. In such fibers, the hollow core is surrounded by a solid multilayer structure consisting of the alternating layers of several materials with distinct refractive indexes. In a specific frequency range, called bandgap, a periodic dielectric multilayer serves as an efficient mirror that confines radiation in the hollow fiber core.

Although refractive-index contrast between layers in an all-polymer Bragg fiber is relatively small (at most 1.3/1.7), as demonstrated in [4], liquid core all-polymer Bragg fibers can be designed to guide very well both TE and TM like modes, while gas-filled all-polymer Bragg fibers can guide effectively a TE polarized mode. We believe that fabrication simplicity and potential biocompatibility of such fibers can be attractive for applications in biomedical sector. Recently, our research group has succeeded in developing two methodologies for fabrication of multilayered all-polymer hollow preforms. One approach uses a consecutive deposition of layers of two different polymers by solvent evaporation on the inside of a rotating polymer cladding tube [8]. Orthogonal solvents were found, and solvent-evaporation process was developed for both Polymethyl methacrylate (PMMA)/Polystyrene (PS) and Polyvinylidene fluoride (PVDF)/Polycarbonate (PC) material combinations. Alternative preform fabrication method uses a corolling of two dissimilar polymer films similarly to [7], where both commercial and home-made films are used. In Fig. 1, we present an example of a hollow Bragg fiber routinely drawn in our group consisting of a 32 PMMA/PS optical layer region surrounded by a 32 layer PMMA ovecladding and a PMMA tube supercladding. Defects and delamination in the overcladding appear during cutting of the fibers and not during drawing process.

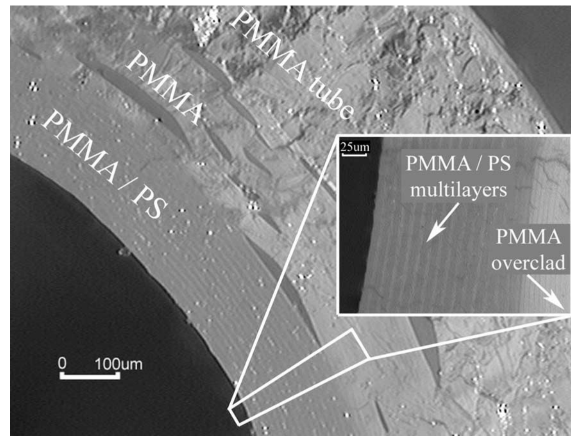

Fig. 1. Example of a hollow Bragg fiber consisting of a 32-PMMA/PS optical layer region surrounded by a PMMA ovecladding and a tube supercladding.

In addition to preform geometry, profile of the drawn fiber can be significantly influenced by the choice of various parameters in the drawing process such as temperature of the furnace, fiber draw and preform feed velocities, and pressurization of a hollow core. The viscoelastic nature of polymeric flow is also of importance for many of the polymer materials used in polymer fiber fabrication (PS, for example). Previous studies on fiber drawing have focused mainly on spinning molten threadlines [9], [10] or drawing conventional solid optical fibers [11], [12]. Melt spinning of viscoelastic liquids is studied in [13] and [14]. Drawing of hollow fibers was first studied in [15] where the asymptotic "thin-filament" equations were obtained, but the effects of surface tension were neglected. A more complete analysis, although confined to Newtonian flow, is given in [16]–[19].

The two-stage draw process is routinely used in the fabrication of the microstructured fibers. First, preforms are drawn into canes with an outside diameter on the order of millimeters. Second, the canes are jacketed by a supercladding and then redrawn into the fibers with diameters on the order of hundreds micrometers. Experiments and theoretical analysis of a thick polymer tube drawing into canes showed that in the regime,

Manuscript received April 7, 2006; revised August 20, 2006. This work was supported by the Canada Research Chair, Canada Institute for Photonics Innovations projects BP5 and FP3, and Strategic NSERC Grant 306667-04.

E. Pone, N. Guo, S. Lacroix, and M. Skorobogatiy are with the Department of Engineering Physics, École Polytechnique de Montréal, Montréal, QC H3C 3A7, Canada (e-mail: maksim.skorobogatiy@polymtl.ca).

C. Dubois is with the Department of Chemical Engineering, École Polytechnique de Montréal, Montréal, QC H3C 3A7, Canada.

Digital Object Identifier 10.1109/JLT.2006.884488

when the effect of surface tension is small, the tube hole has a tendency to expand [18]–[20]. In contrast, when drawing thin polymer tubes, the hole collapse was always observed [16]. During the following redrawing of canes wrapped into a supercladding, where small features (high curvature) are present in the preform cross section and relatively high temperatures (low viscosity) are used, the surface-tension force can be of importance, and it can cause a partial or even complete collapse of the hollow microstructure. Note that the hole collapse affects not only the ratio between the inner and outer diameters of a fiber, but it also affects the thickness of the reflector layers, both factors having an impact on the fiber-transmission properties. The purpose of this paper is to characterize such a hole collapse and nonuniformity in the reflector during the drawing of the viscoelastic hollow fibers when the surface-tension effects are nonnegligible. In particular, we investigate how the hole collapse is affected by the control parameters in the drawing process and how it affects the fiber transmission.

The flow parameters are temperature dependent, and the drawing process relies on the heat transfer within the furnace. We have chosen to take a simple point of view by considering the isothermal drawing of the hollow fibers, thus avoiding the heat-transfer analysis. Furthermore, the choice of an isothermal case makes it easier for the rheological characterization of the viscoelastic liquid. The choice of the constitutive equation relating stress to deformation is an essential difficulty in analyzing the polymeric flow. There is always a compromise between the generality of stress equation and the ease of solution. The type of the process involved imposes restrictions on the class of constitutive equations which can be considered. Fiber drawing can be a high Deborah number process where the residence time is comparable to the fluid relaxation time. For such a process, the stress equation must account for the liquid memory over the entire process time. The dependence of the viscosity on the deformation is also an important factor in polymeric flow. The simplest isothermal constitutive equation, which accounts for the shear thinning of the viscosity and is valid for high Deborah number processes, is the White-Metzner model [14], [21]. A more general derivative of this model is considered in this paper. All the numerical codes used in this paper can be found at our group web site.

II. Flow Equations and Boundary Conditions

A schematic of a hollow multilayer preform profile during drawing is shown in Fig. 2 (right). For an incompressible axisymmetric steady flow, the equations for conservation of mass and momentum in cylindrical coordinates are as follows:

$$\frac{1}{r}\frac{\partial(rv_r)}{\partial r}+\frac{\partial v_z}{\partial_z}=0 \tag{1}$$

$$\begin{aligned}\rho\left(v_r\frac{\partial v_r}{\partial r}+v_z\frac{\partial v_r}{\partial z}\right) &= -\frac{\partial p}{\partial r}+\frac{1}{r}\frac{\partial(r\tau_{rr})}{\partial r} - \frac{\tau_{\theta\theta}}{r}+\frac{\partial \tau_{rz}}{\partial z}\\ \rho\left(v_r\frac{\partial v_z}{\partial r}+v_z\frac{\partial v_z}{\partial z}\right) &= -\frac{\partial p}{\partial z}+\frac{1}{r}\frac{\partial(r\tau_{rz})}{\partial r} + \frac{\partial \tau_{zz}}{\partial z}+\rho g\end{aligned} \tag{2}$$

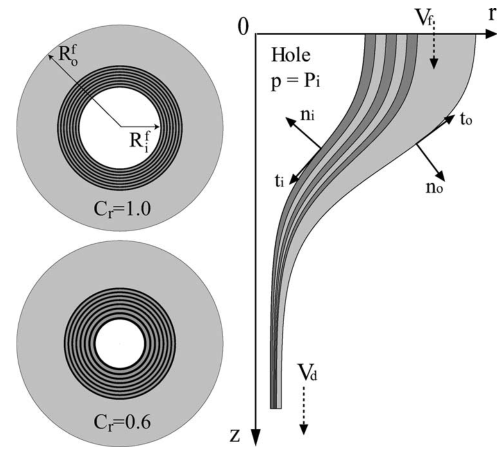

Fig. 2. (Left) Examples of drawing without $C_r = 1$ and with hollow core collapse $C_r = 0.6$ for the same value of the outside fiber radius $R_{\mathrm{o}}^{\mathrm{f}}$. (Right) Schematic of a hollow multilayer preform during drawing.

where r and z are the radial and axial coordinates, v_r and v_z are the r and z components of the velocity vector $\mathbf{v}$, ρ is the constant density, p the pressure, τ_{ij} is the extra stress, and g is the gravitational acceleration. The components of the total stress tensor $\bar{\bar{\sigma}}$ are

$$\sigma_{ij}=-p\delta_{ij}+\tau_{ij}. \tag{3}$$

The constitutive equation for τ_{ij} is considered later. For these equations, the boundary conditions must be specified. At the interfaces between different layers, the kinematic conditions (steady flow) are

$$v_r=R_j'v_z \quad \text{at} \quad r=R_j \tag{4}$$

where $R_j = R_j(z)$ denote the interfaces between layers and the index $j = 1, 2 \ldots N$ is used to number them starting from the inner one. The primes denote the derivative with respect to z. Since the first and the Nth interfaces are external interfaces, we will distinguish them by denoting $R_i \equiv R_1$ and $R_{\mathrm{o}} \equiv R_N$ for the inner and outer boundaries, respectively.

Hollow core can also be pressurized in order to control its collapse under the action of the surface tension. In this case, at the inner interface, the dynamic boundary conditions are

$$\begin{aligned}\bar{\bar{\sigma}}\cdot\mathbf{n_i}&=(\gamma\kappa_i-P_i)\mathbf{n_i}\\ \bar{\bar{\sigma}}\cdot\mathbf{t_i}&=\mathbf{0}\end{aligned} \tag{5}$$

where γ denotes the surface-tension coefficient

$$\kappa_i=\frac{1}{R_i\left(1+{R_i'}^2\right)^{1/2}}-\frac{R_i''}{\left(1+{R_i'}^2\right)^{3/2}}$$

is the curvature, and P_i is the hole overpressure (the constant ambient pressure has no effect on the flow). Outward-pointing normal at the inner boundary $\mathbf{n_i}$ is defined as

$$\mathbf{n_i^{\mathrm{T}}}=(n_r,n_\theta,n_z)=\left(-\frac{1}{\sqrt{1+{R_i'}^2}},0,\frac{R_i'}{\sqrt{1+{R_i'}^2}}\right) \tag{6}$$

while

$$\mathbf{t_i}^{\mathrm{T}} = (n_z, 0, -n_r) \tag{7}$$

is the unit tangent vector. In a similar way, the dynamic boundary conditions at the outer boundary are

$$\begin{aligned} \bar{\bar{\sigma}} \cdot \mathbf{n_o} &= -\gamma\kappa_o \mathbf{n_o} \\ \bar{\bar{\sigma}} \cdot \mathbf{t_o} &= 0 \end{aligned} \tag{8}$$

where $\mathbf{n_o}$, $\mathbf{t_o}$, and κ_o satisfy the same equations as $-\mathbf{n_i}$, $-\mathbf{t_i}$, and κ_i, respectively, with R_i replaced by R_o.

At the internal interfaces between layers, a continuous stress and velocity and a negligible surface tension are considered. In the axial direction, the boundary conditions are the known values of the draw (V_d) and the feed (V_f) velocities. Furthermore, as an initial condition, the values $R_j(0)$ are known.

III. Thin-Filament Equations

One of the basic dimensionless parameters in the problem is a ratio ϵ between the preform radius and the length of a neck down region. In the case when $\epsilon \ll 1$, a thin-filament approximation can be used. There are two different approaches for simplifying the equations in this case. In the first one [17], [22], the variables are expanded as power series in ϵ^2 and only the dominant terms are retained in the equations. In the second one [15], which we use in this paper, the equations are averaged over the cross section at each value of z.

The average $\overline{\varphi}(z)$ of a variable $\varphi(z)$ is defined as

$$\overline{\varphi}(z) = \frac{1}{\pi\left(R_o^2 - R_i^2\right)} \int_{R_i}^{R_o} 2\pi r \varphi(r,z) dr. \tag{9}$$

For the axial velocity, the assumption $v_z = \overline{v}_z$ is made explicitly. It can be noted first that for a slow-varying thin filament; $R'_j \ll 1$. Thus, by neglecting terms of the order ${R'_j}^2$, the boundary conditions (5) and (8) take the following form:

$$\begin{aligned} \sigma_{rr} &= \frac{\gamma}{R_i} - P_i \\ \sigma_{rz} &= \left(-\frac{\gamma}{R_i} + P_i\right) R'_i \qquad \text{at} \quad r = R_i \\ \sigma_{zz} &= \left(\frac{\gamma}{R_i} - P_i\right) {R'_i}^2 \\ \sigma_{rr} &= -\frac{\gamma}{R_o} \\ \sigma_{rz} &= \frac{\gamma}{R_o} R'_o \qquad\qquad \text{at} \quad r = R_o \\ \sigma_{zz} &= -\frac{\gamma}{R_o} {R'_o}^2. \end{aligned} \tag{10}$$

Multiplying the r-component of the momentum (2) by $2\pi r^2$, integrating from R_i to R_o, considering $(d/dz) \int_{R_i}^{R_o} 2\pi r^2 \tau_{rz} dr \approx 0$, neglecting the inertial term because of the small value of the radial velocity and using the boundary values of σ_{rr} given by (10), the following relation is obtained:

$$\overline{p} = \frac{\overline{\tau}_{rr} + \overline{\tau}_{\theta\theta}}{2} + \frac{\gamma(R_o + R_i) - R_i^2 P_i}{R_o^2 - R_i^2}. \tag{11}$$

Multiplying the z-component of the momentum (2) by $2\pi r$, integrating from R_i to R_o, using the boundary values of $\tau_{rz} = \sigma_{rz}$ given by (10) and (11) and neglecting terms of relative order ${R'_j}^2$, one finds

$$\overline{\rho} Q v'_z = \left[\frac{Q}{v_z}\left(\overline{\tau}_{zz} - \frac{\overline{\tau}_{rr} + \overline{\tau}_{\theta\theta}}{2}\right) + \pi\gamma(R_o + R_i)\right]' + \overline{\rho} g \frac{Q}{v_z} \tag{12}$$

where $Q = \pi(R_o^2 - R_i^2)v_z$ is the constant volumetric flow rate. This is the axial force balance equation.

Usually, in the fiber-drawing process, the inertial, capillary, and gravitational terms are negligible compared to viscoelastic stresses, and the axial force balance takes the simple form

$$\left[\frac{1}{v_z}\left(\overline{\tau}_{zz} - \frac{\overline{\tau}_{rr} + \overline{\tau}_{\theta\theta}}{2}\right)\right]' = 0. \tag{13}$$

IV. Constitutive Equation

The constitutive equation relates stress to deformation. For the Newtonian fluid, it is given by

$$\tau = 2\eta_0 D \tag{14}$$

where τ is the stress tensor, η_0 the viscosity, and D is the deformation tensor. In cylindrical coordinates and for an axially symmetric flow, the deformation tensor has the form

$$D = \frac{\nabla \mathbf{v} + \nabla \mathbf{v}^{\mathrm{T}}}{2} = \begin{pmatrix} \frac{\partial v_r}{\partial r} & 0 & 0 \\ 0 & \frac{v_r}{r} & 0 \\ 0 & 0 & v'_z \end{pmatrix}. \tag{15}$$

Here, the components $D_{rz} = D_{zr} = \partial v_r / \partial z$ are neglected because in the thin-filament approximation, they are of order ϵ compared to the diagonal terms [21, p. 382]. Drawing of multilayer fibers made of polymers exhibiting pure Newtonian flow has been detailed in our previous work [16].

Polymeric flow is typically non-Newtonian. The first complication arises from the fact that polymer viscosity depends on kinematics of the flow and more precisely on the second invariant of a deformation tensor defined as

$$II_D = \sqrt{2\,\text{trace}(D \cdot D)}. \tag{16}$$

From the continuity equation, one finds

$$\frac{\partial v_r}{\partial r} = -\frac{1}{2}v'_z - \frac{A}{r^2} \qquad \frac{v_r}{r} = -\frac{1}{2}v'_z + \frac{A}{r^2} \tag{17}$$

where $A = A(z)$ is a function discussed in more details later. In most cases of practical importance $A/r^2 \ll v'_z$, and the second invariant of a deformation tensor is simply given by

$$II_D = \sqrt{3} v'_z. \tag{18}$$

We choose the form of a deformation rate-dependent viscosity as in [23]:

$$\eta(II_D) = \frac{\eta_0}{1 + (K_1 II_D)^n} \tag{19}$$

where η_0 is the Newtonian viscosity, K_1 is a parameter with the dimension of time, and n is a constant. This is known as the Cross model, and it is able to describe the flow of a wide range of non-Newtonian liquids [24]. A corresponding equation for the stress, which is also known as the generalized Newtonian model, then becomes

$$\tau = 2\eta(II_D)D. \tag{20}$$

In addition to having a non-Newtonian viscosity polymers can be strongly elastic exhibiting a so-called viscoelastic flow. Effect of elasticity can be accounted for in the constitutive equation by adding the time derivative of the stress tensor. As the drawing of the hollow Bragg fibers involves large displacement gradients in the axial direction, in this case, the time derivative of the stress tensor must be replaced by a special time derivative known as the convected time derivative, and the corresponding viscoelastic model is called nonlinear [21]. In this paper, we tackle the simplest of the nonlinear viscoelastic models called the White–Metzner model [21], [23]

$$\tau + \lambda(II_D)\overset{\nabla}{\tau} = 2\eta(II_D)D \tag{21}$$

where deformation rate-dependent parameter λ is called the relaxation time (unit s), and $\overset{\nabla}{\tau}$ is a convected time derivative of the stress tensor defined as [21]

$$\overset{\nabla}{\tau} = \frac{\partial \tau}{\partial t} + \mathbf{v}\cdot\nabla\tau - \nabla\mathbf{v}\cdot\tau - \tau\cdot\nabla\mathbf{v}^{\mathrm{T}} \tag{22}$$

where the superscript $^{\mathrm{T}}$ denotes the transpose vector. The form of $\lambda(II_D)$ considered by us is the one presented in [23].

$$\lambda(II_D) = \frac{\lambda_0}{1 + K_2 II_D} \tag{23}$$

where λ_0 and K_2 are constant parameters with the dimension of time. This particular form of the relaxation time is used because it avoids the infinite values of extensional viscosity and because it has been successful in describing the $\lambda(II_D)$ curves for a wide range of viscoelastic liquids [23].

For an axially symmetric flow in cylindrical coordinates and for the steady-state regime, the components of (21) take the form

$$\begin{aligned}
\tau_{rr} + \lambda(II_D)\left(v_r\frac{\partial \tau_{rr}}{\partial_r} + v_z\tau'_{rr} - 2\tau_{rr}\frac{\partial v_r}{\partial_r}\right) &= 2\eta(II_D)\frac{\partial v_r}{\partial_r}\\
\tau_{\theta\theta} + \lambda(II_D)\left(v_r\frac{\partial \tau_{\theta\theta}}{\partial_r} + v_z\tau'_{\theta\theta} - 2\tau_{\theta\theta}\frac{v_r}{r}\right) &= 2\eta(II_D)\frac{v_r}{r}\\
\tau_{zz} + \lambda(II_D)\left(v_r\frac{\partial \tau_{zz}}{\partial_r} + v_z\tau'_{zz} - 2\tau_{zz}v'_z\right) &= 2\eta(II_D)v'_z.
\end{aligned} \tag{24}$$

It is seen that the viscoelastic model is much more complex than the generalized Newtonian model, because the constitutive equation is a differential equation for τ.

V. Axial Velocity

We define R_i^{f} and $R_{\mathrm{o}}^{\mathrm{f}}$ to be the inside and outside radii of the drawn hollow fiber while R_i^p and R_{o}^p are the corresponding radii of the hollow preform. A parameter that relates preform and fiber dimensions is a drawdown ratio D_{d} which is defined as a ratio of the outside preform diameter to that of a fiber $D_{\mathrm{d}} = R_{\mathrm{o}}^p/R_{\mathrm{o}}^{\mathrm{f}}$. Drawdown ratio can be set during drawing process, and it is typically well maintained by a feedback loop from a laser micrometer to a tractor assembly. To simplify the calculations, instead of a fixed drawdown ratio, we consider a fixed draw ratio defined as $D_r = V_{\mathrm{d}}/V_{\mathrm{f}}$. This makes the evaluation of the axial velocity easier by uncoupling it from the cross-sectional profile. If calculations for a fixed D_{d} are needed, the complete solution procedure (axial velocity + cross-sectional profile) described in what follows can still be used but in an iterative way, that is D_r must be varied until the condition for the desired D_{d} is met.

A. Generalized Newtonian Model

In this section, we consider in more details the generalized Newtonian model. Note that the Newtonian model is a subcase of the generalized model, i.e., it can be obtained by setting $K_1 = 0$ in (19). When (17) is substituted into the deformation tensor (15), which is, in turn, substituted into the constitutive (20), and after averaging, the following is obtained:

$$\overline{\tau}_{zz} - \frac{\overline{\tau}_{rr} + \overline{\tau}_{\theta\theta}}{2} = 3\overline{\eta}v'_z. \tag{25}$$

Thus, the axial balance (13) takes a simple form

$$\overline{\eta}\frac{v'_z}{v_z} = C \tag{26}$$

where C is a constant. This equation can be easily integrated

$$v_z(z) = \exp\left(\ln V_{\mathrm{f}} + \frac{\int_0^z \frac{dz}{\overline{\eta}(z)}}{\int_0^L \frac{dz}{\overline{\eta}(z)}}\ln\frac{V_{\mathrm{d}}}{V_{\mathrm{f}}}\right) \tag{27}$$

where L is a furnace length.

B. Viscoelastic Model

The stress components vary little in the radial direction. We will still quantify this variation in the next section as it is important for the development of a cross-sectional profile. However, for the evaluation of the axial velocity, we may simply consider

$$\tau_{\phi\phi}(r) \approx \overline{\tau}_{\phi\phi} \tag{28}$$

where ϕ represents any of the coordinates r, θ, and z. By taking the average over cross-sectional value in both sides of (24) and taking into account (17), (28), and the fact that $A/r^2 \ll v_z'$, the constitutive equations assume the form

$$\begin{aligned}\overline{\tau}_{xx} + \overline{\lambda}\left(v_z\overline{\tau}_{xx}' + v_z'\overline{\tau}_{xx}\right) &= -\overline{\eta}v_z'\\ \overline{\tau}_{zz} + \overline{\lambda}\left(v_z\overline{\tau}_{zz}' - 2v_z'\overline{\tau}_{zz}\right) &= 2\overline{\eta}v_z'\end{aligned} \tag{29}$$

where x stands for both r and θ. Averaging of the relaxation time and viscosity reflects the multilayer structure of a cross section (layers with different λ_0, K_2, η_0, K_1, and n).

Equations (29) and (13) form a system of three coupled differential equations with respect to the three unknown z dependent functions $(v_z, \overline{\tau}_{zz}, \overline{\tau}_{xx})$. These equations are similar to the equations obtained in [14] for the spinning of solid thin filaments. The main difference in our case is the fact that the fiber fabrication consists of drawing a heated preform, and no extrusion is present. This fact only affects the initial $(z = 0)$ values of $\overline{\tau}_{zz}$ and $\overline{\tau}_{xx}$, although in [14], it is observed that the axial velocity field is insensitive to these initial values. In our case, at $z = 0$, there is no deformation history and the elasticity term must be ignored ($\lambda = 0$ so that $\overline{\tau}_{zz}(0) - \overline{\tau}_{xx}(0) = 3\overline{\eta}(0)v_z'(0)$). With this slight modification, the system of (13) and (29) can be solved by using the same iterative procedure as the one described in [14]. Thus, the three equations are combined into a single differential equation with respect to v_z and unknown constant C. Starting from the initial value V_f and any value of C, a solution can be obtained along z-axis. C is varied until the correct value of velocity $v_z(L) = V_\mathrm{d}$ is obtained at $z = L$.

VI. Cross-Sectional Profile

Combining (4) with (17), the following equation is obtained for the interfaces between different layers:

$$\left(R_j^2 v_z\right)' = 2A. \tag{30}$$

The initial values $R_j(0)$ (the preform configuration) are known, and the axial velocity $v_z(z)$ can be determined by an uncoupled procedure. Thus, by integrating (30) along the z-axis, the cross-sectional profile can be determined provided that $A(z)$ is known. From this equation, it also follows that the ratio of areas of two different layers is conserved along z-axis.

Integrating the r-component of the momentum (2) from R_i to R_o, neglecting the inertial term, and using the boundary values of σ_{rr} given by (10), we obtain

$$P_i - \gamma\left(\frac{1}{R_i} + \frac{1}{R_\mathrm{o}}\right) + \int_{R_i}^{R_\mathrm{o}} \frac{\tau_{rr} - \tau_{\theta\theta}}{r} dr = 0. \tag{31}$$

This important equation can be exploited to evaluate $A(z)$. The integration of (30) and the evaluation of $A(z)$ are done simultaneously. In the following, the evaluation procedure for $A(z)$ is presented for both models.

A. Generalized Newtonian Model

From (15), (17), and (20), it follows that

$$\tau_{rr} - \tau_{\theta\theta} = 4\eta\frac{A}{r^2}. \tag{32}$$

Substituting this result into (31), the following is obtained:

$$A = \frac{P_i - \gamma\left(\frac{1}{R_i} + \frac{1}{R_\mathrm{o}}\right)}{4\int_{R_i}^{R_\mathrm{o}} \frac{\eta(r)}{r^3} dr}. \tag{33}$$

B. Viscoelastic Model

We consider a steady-state solution for which any streamline $r(z)$ in the material would satisfy (30) with $R_j(z)$ replaced by $r(z)$. In a Lagrangian point of view, two neighboring positions along the same streamline would then be related by

$$\frac{r(z+dz)^2 v_z(z+dz) - r(z)^2 v_z(z)}{dz} = 2A(z). \tag{34}$$

Suppose that at a given z, the cross-sectional profile $R_j(z)$, radial distributions $\tau_{rr}(r,z)$, and $\tau_{\theta\theta}(r,z)$ and $A(z)$, are known and we want to advance the solution to $z + dz$.

We first substitute (17) into (24) to obtain

$$\begin{aligned}\tau_{rr} + \lambda\left[\frac{D\tau_{rr}}{Dt} - 2\tau_{rr}\left(-\frac{1}{2}v_z' - \frac{A}{r^2}\right)\right] &= 2\eta\left(-\frac{1}{2}v_z' - \frac{A}{r^2}\right)\\ \tau_{\theta\theta} + \lambda\left[\frac{D\tau_{\theta\theta}}{Dt} - 2\tau_{\theta\theta}\left(-\frac{1}{2}v_z' + \frac{A}{r^2}\right)\right] &= 2\eta\left(-\frac{1}{2}v_z' + \frac{A}{r^2}\right).\end{aligned} \tag{35}$$

Here, we have used the material derivative $D\tau_{xx}/Dt = v_r(\partial\tau_{xx}/\partial r) + v_z\tau_{xx}'$ because it is more convenient for free surfaces. The discretized form of the material derivative is given by

$$\frac{D\tau_{xx}}{Dt} = \frac{\tau_{xx}\left[r(z+dz)\right] - \tau_{xx}\left[r(z)\right]}{dt} \tag{36}$$

where $dt = dz/v_z(z)$ and $r(z + dz)$ and $r(z)$ are related by (34). Substituting (36) into (35) applied at $z + dz$, the stress components in the form of relations $\tau_{rr}[r(z+dz), A(z+dz)]$, and $\tau_{\theta\theta}[r(z+dz), A(z+dz)]$ are obtained. Finally, by substituting these relations into (31), $A(z + dz)$ can be evaluated. In this way, we can advance the solution along the z-axis. At $z = 0$, the elasticity term must be neglected and the relation for $A(0)$ is simply given by (33).

VII. Hole Collapse in a Drawn Tube

In this section, we consider drawing of a single material tube to investigate the effect of different draw parameters. As an example, we consider drawing of a PS capillary which is a viscoelastic polymer and is one of the materials that we use in the fabrication of Bragg fibers. We consider a preform tube with an outer radius $R_\mathrm{o}^p = 1$ mm and an inner one $R_i^p = 0.8$ mm. The furnace length is considered $L = 20$ cm. The temperature inside the furnace is constant and equal to

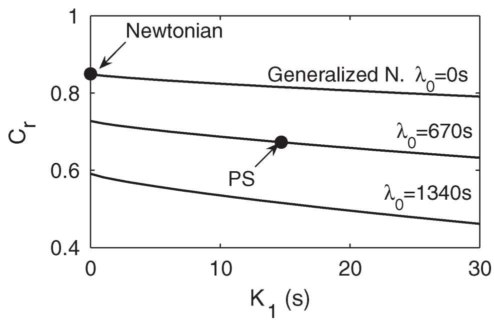

Fig. 3. Effects of the non-Newtonian viscosity and elasticity on hole collapse. Draw parameters are $T = 170$ °C, $V_{\mathrm{f}} = 50$ μm/s, $D_r = 25$, and $P_i = 0$ Pa.

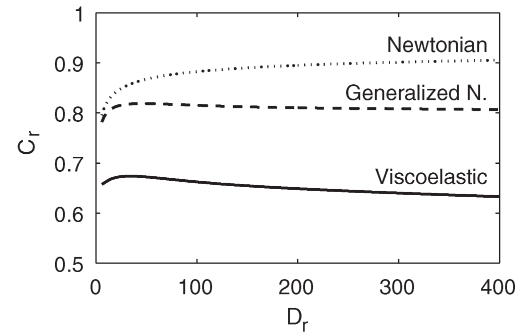

Fig. 4. Effect of the draw ratio on the hole collapse. Draw parameters are $T = 170$ °C, $V_{\mathrm{f}} = 50$ μm/s, and $P_i = 0$ Pa.

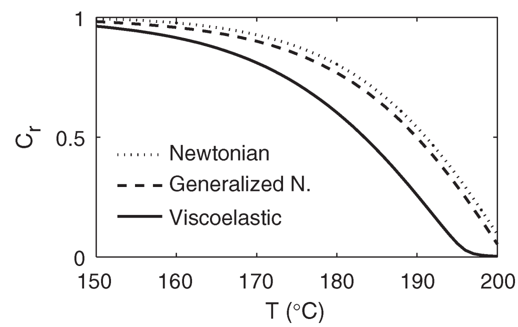

Fig. 5. Effect of the drawing temperature on the hole collapse. Draw parameters are $V_{\mathrm{f}} = 100$ μm/s, $D_r = 25$, and $P_i = 0$ Pa.

$T = 170$ °C. Furthermore, we assume a feed velocity $V_{\mathrm{f}} = 50$ μm/s, a draw ratio $D_r = 25$, and a zero hole overpressure $P_i = 0$ Pa. The flow parameters of PS at $T = 170$ °C are given in [23]: $\lambda_0 = 670$ s, $K_2 = 1000$ s, $\eta_0 = 4.791 \cdot 10^5$ Pa $\cdot$ s, $K_1 = 14.7$ s and $n = 0.799$. According to [25], the surface tension of PS at $T = 170$ °C is $\gamma = 0.03$ N/m.

To characterize the hollow core collapse in the fiber, we introduce a parameter defined as $C_r = (R_i^{\mathrm{f}}/R_{\mathrm{o}}^{\mathrm{f}})/(R_i^p/R_{\mathrm{o}}^p)$. Thus, $C_r = 0$ signifies that during drawing, fiber core collapses completely resulting in a solid core fiber, while $C_r = 1$ signifies that there is no hole collapse and all the fiber dimensions can be calculated from the corresponding preform dimensions by a simple division by a drawdown ratio [see Fig. 2 (left)]. By solving the viscoelastic model as explained in the previous section using the material parameters given above, the value $C_r = 0.67$ of core collapse is obtained, signifying a considerable hole collapse during drawing.

We begin our analysis by investigating how the presence of elasticity and non-Newtonian viscosity affects the hole collapse. This is done by plotting the hole-collapse parameter C_r as a function of K_1 for different values of λ_0, keeping the other material parameters unchanged. Such plots are presented in Fig. 3. Note that the case of $K_1 = 0$, $\lambda_0 = 0$ corresponds to a Newtonian model, while the case of $K_1 > 0$, $\lambda_0 = 0$ corresponds to a generalized Newtonian model. It is seen that the presence of both non-Newtonian (shear thinning) viscosity and elasticity increases the hole collapse. When K_1 is increasing, the viscosity is decreasing, and this results in a more pronounced hole collapse. The role of elasticity is somewhat counterintuitive, since it is expected that its presence would make the liquid tend to retreat to its initial position, thus resulting in less of a hole collapse. Detailed simulations show that this is indeed the case in a two-dimensional case when a uniformly heated tube in the absence of any external stresses collapses under the force of a surface tension. However, in a three-dimensional case corresponding to fiber drawing, when the structure is stretched and the overall stresses are higher, the presence of elasticity works in favor of the hole collapse.

In what follows, Newtonian model assumes the PS material parameters mentioned above with $K_1 = 0$ and $\lambda_0 = 0$, while generalized Newtonian model only assumes that $\lambda_0 = 0$.

Next, we consider the effect of the drawing process parameters: draw ratio, furnace temperature, feed speed, and hole pressure. The effect of draw ratio D_r is presented in Fig. 4. It is seen that the hole collapse is not affected significantly by the draw ratio. Starting with preforms of the same diameter, the draw-ratio increase leads to the reduction of a resultant fiber cross section. As a consequence, the forces of surface tension become more pronounced, thus favoring the hole collapse. This is compensated by the fact that increasing the draw ratio leads to the higher axial velocities; thus, the time a cross section spends in a melted zone diminishes which works against the hole collapse.

The effect of temperature is considered by using the Williams–Landel–Ferry shift factor [26]. According to this theory, if the values of η_0, λ_0, K_1, and K_2 are known at a reference temperature T_0 near the glass transition temperature T_{g}, the corresponding values at a temperature T are given by $\eta_0 a_T$, $\lambda_0 a_T$, $K_1 a_T$, and $K_2 a_T$, where the shift factor a_T is calculated by the following relation:

$$\log_{10} a_T = \frac{-C_1^0 (T - T_0)}{C_2^0 + (T - T_0)} \qquad (37)$$

where C_1^0 and C_2^0 are two constants. This formula is valid in the range T_{g} to about $T_{\mathrm{g}} + 100$. For PS $(T_{\mathrm{g}} = 97\ ^\circ\mathrm{C})$ at the reference temperature $T_0 = 100$ °C, the values of constants are $C_1^0 = 12.7$ and $C_2^0 = 49.8$ °C [26]. Since the shifted values of η_0, λ_0, K_1, and K_2 at $T = 170$ °C are known for PS, the unshifted ones at T_0 can be evaluated and then used to calculate polymer material parameters at any temperature. In Fig. 5, the effect of temperature on the hole collapse is presented. It shows that the hole collapse increases as the drawing temperature increases. This is attributed to the decrease in the viscosity

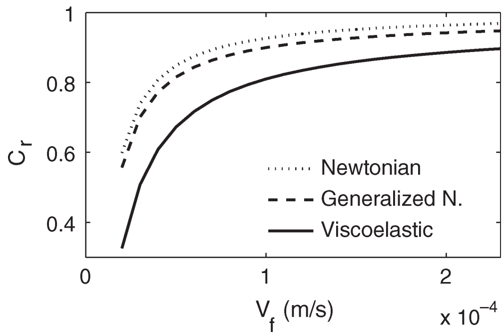

Fig. 6. Effect of the feeding velocity on the hole collapse. Draw parameters are $T = 170$ °C, $D_r = 25$, and $P_i = 0$ Pa.

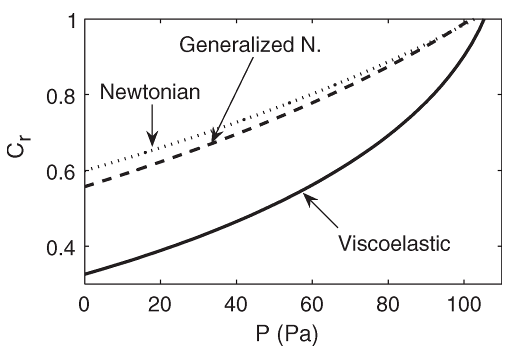

Fig. 7. Effect of hole overpressure on the hole collapse. Draw parameters are $T = 170$ °C, $V_{\rm f} = 20$ μm/s, and $D_r = 25$.

$\eta(II_D)$, which is strong enough to overcompensate the inverse effect of $\lambda(II_D)$.

Next, the effect of feeding velocity is considered. In Fig. 6, the hole-collapse parameter C_r is presented as a function of $V_{\rm f}$ keeping all the other draw parameters constant. We note that by increasing $V_{\rm f}$, the hole collapse is reduced, but it cannot be avoided. By changing strongly for small values of $V_{\rm f}$, C_r remains almost constant when $V_{\rm f}$ is further increased. Thus, if one already works in the almost horizontal part of the curve in Fig. 6, the increase of the feed velocity will not reduce further the hole collapse. Furthermore, the increase in feed velocity has its limits. For a given draw ratio, this limit is fixed by the maximum draw velocity attainable by the tractor and spooler assembly.

Finally, the effect of hole overpressure is studied. We consider the case when a considerable hole collapse takes place ($V_{\rm f} = 20$ μm/s; minimum feed velocity in the previous graph), and investigate if by adding some overpressure, it could be avoided. In Fig. 7, C_r as a function of P_i is presented. We remark that the hole collapse can be avoided by pressurizing the hole. However, calculations show that no solution is obtained if the overpressure is higher than a certain critical value (108 Pa in this particular case), which suggests that the drawing process cannot reach the steady-state regime. Thus, the hole pressurization must be handled with care.

In all the cases presented above, we note small difference between the results attained by Newtonian and generalized Newtonian models, which however, differ considerably from the results attained by the viscoelastic polymer flow model.

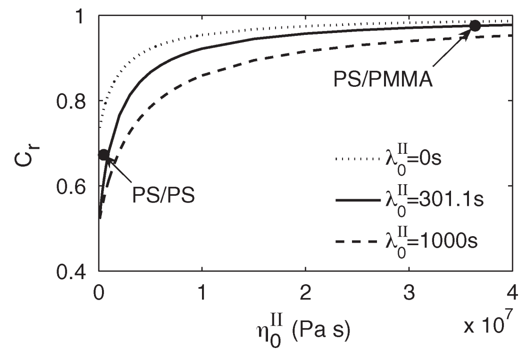

Fig. 8. Effect on the hole collapse of the viscosity and elasticity parameter mismatch between the materials in a multilayer structure.

VIII. Hole Collapse and Layers Nonuniformity in a Drawn Bragg Fiber

For a multilayer fiber, solution procedure remains essentially the same as for a single material tube. The effect of draw parameters on the hole collapse is basically the same as in the case of a tube. Consider, for example, a preform composed of a bulk tube of PS containing on the inside a number of thin alternating layers of PS and some other polymer [Fig. 2 (left)]. What is interesting to study in this case is how the material parameters of the second polymer affect the hole collapse even as this polymer accounts only for a small fraction of the total volume.

As an example, we consider again the same drawing recipe as in the previous section, that is, $T = 170$ °C, $L = 20$ cm, $V_{\rm f} = 50$ μm/s, $D_r = 25$, and $P_i = 0$ Pa. The outer and inner radii of a capillary preform are the same as in the case of a single material tube $R_{\rm o} = 1$ mm, $R_{\rm o} = 0.8$ mm. What is different this time is the cladding tube inner radius $R_i = 0.9$ mm and the presence of 20 alternated layers of PS and another polymer. The thickness of each layer is considered 5 μm; therefore, overall, the thickness of the multilayer structure plus the cladding tube is the same as the thickness of the tube studied before. Thus, when the second polymer is PS, the drawing results in a hole-collapse parameter $C_r = 0.67$. To investigate how C_r is affected by the different viscosity (η^{II}) and elasticity (λ^{II}) of the second polymer, we will simply vary the corresponding zero shear-rate values η_0^{II} and λ_0^{II}.

The flow parameters of the second polymer are chosen to correspond to the ones of PMMA, which is another polymer used in our fabrication of polymer Bragg fibers. The flow parameters for PMMA at $T = 190$ °C are given in [23]: $\lambda_0 = 1.039$ s, $K_2 = 1.384$ s, $\eta_0 = 1.255 \cdot 10^5$ Pas, $K_1 = 0.9088$ s, and $n = 0.5776$. These values, except for n, must be shifted to 170 °C. This can be done in the same way as in the previous section, considering that for PMMA at the reference temperature $T_0 = 115$ °C, the shift constants are $C_1^0 = 32.2$ and $C_2^0 = 80$ °C [26].

In Fig. 8, variation of C_r as a function of η_0^{II} is presented for different values of λ_0^{II}. We remark that the hole collapse depends significantly on the viscosity of the second polymer and, to a lesser extent, on its elasticity, despite the fact that the second polymer occupies only a small fraction (23%) of the overall volume of a preform.

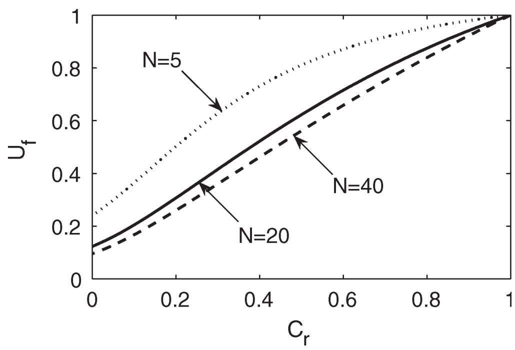

Fig. 9. Layers nonuniformity parameter as a function of the hole collapse.

The hole collapse also affects the uniformity of the layer thicknesses. The hole collapse typically results in a faster reduction of an inner radius compared to an outer one. Thus, in the drawn fiber, the inner layers will become thicker than the outer ones even if in the preform they had the same thickness. We will characterize the thickness nonuniformity of an initially periodic multilayer structure by the parameter U_{f} defined as the ratio between the thickness of the outer layer and the thickness of the inner one $U_{\mathrm{f}} = d_{\mathrm{o}}/d_i$. Thus, $U_{\mathrm{f}} = 1$ corresponds to a uniform multilayer, while $U_{\mathrm{f}} < 1$ signifies nonuniformity in the multilayer structure. Since the area ratios between any two layers are conserved along z-axis (mass conservation), the uniformity parameter depends only on the hole-collapse parameter and the initial configuration of the layers in the preform. Thus, a circular contour of radius r^p in a preform translates into a circular contour of radius r^{f} in a fiber, which are related by

$$(r^{\mathrm{f}})^2 = \left(\frac{r^p}{D_{\mathrm{d}}}\right)^2 - \left(1 - C_r^2\right)\left(\frac{R_i^p}{D_{\mathrm{d}}}\right)^2 \frac{(R_{\mathrm{o}}^p)^2 - (r^p)^2}{(R_{\mathrm{o}}^p)^2 - (R_i^p)^2}. \quad (38)$$

Using this relation and the given preform dimensions, U_{f} can be easily related to C_r. In Fig. 9, layer nonuniformity U_{f} is presented for the preform configuration described above. In the same figure, we also present the curves for $N = 5$ and $N = 40$ layers, keeping layer thicknesses in a preform the same as for $N = 20$. We remark that for a relatively high number of layers, relation between U_{f} and C_r is almost linear and not significantly sensitive to N.

IX. Effect of the Hole Collapse on the Bragg Fiber Optical Properties

To understand the effect of the hole collapse on the transmission properties of the resultant fibers, in Fig. 10, we present a set of theoretical curves showing radiation losses of the TE_{01} core modes for the fibers drawn with different values of C_r while featuring the same outside diameter $R_{\mathrm{o}}^{\mathrm{f}}$. In this example, $C_r = 1$ corresponds to a target hollow core fiber $n_c = 1$ with a strictly periodic 15 layer quarter-wave reflector having material refractive indexes $n_{\mathrm{h}} = 2.0$, $n_{\mathrm{l}} = 1.5$, and layer thicknesses $d_{\mathrm{h}}^t = 0.25\lambda_c^t/\sqrt{n_{\mathrm{h}}^2 - n_c^2} = 144$ nm, $d_{\mathrm{l}}^t = 0.25\ \lambda_c^t/\sqrt{n_{\mathrm{l}}^2 - n_c^2} = 224$ nm, where $\lambda_c^t = 1\ \mu$m. Target fibers inside and outside radii are chosen to be $R_i^{\mathrm{ft}} = 5\ \mu$m, $R_{\mathrm{o}}^{\mathrm{ft}} = 12.72\ \mu$m. By design, such a fiber has a

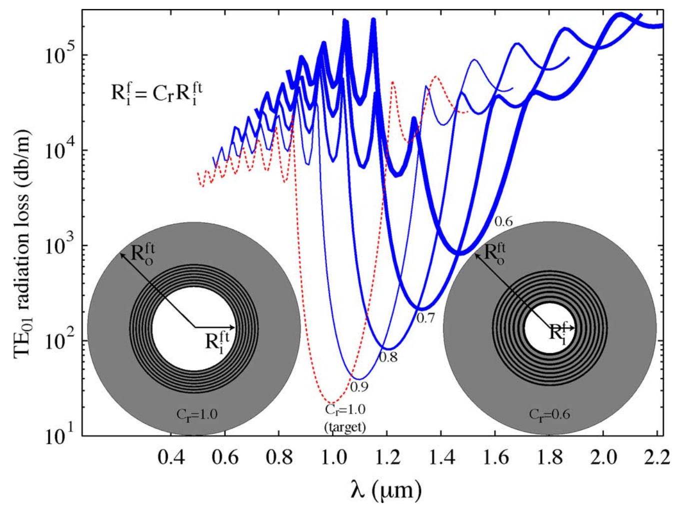

Fig. 10. Radiation loss of the bandgap guided TE_{01} core modes for the fibers with different hole-collapse ratios C_r, while the same are outside radii $R_{\mathrm{o}}^{\mathrm{ft}}$. Core collapse leads to the shift of a bandgap center into the longer wavelength, as well as to a considerable increase in the modal radiation losses. (Color version available online at http://ieeexplore.ieee.org.)

large bandgap centered at λ_c^t. (For more details on the design of high index-contrast hollow Bragg fibers, see [27].) Design of low index-contrast hollow Bragg fibers is detailed in [4], while influence of a core collapse on its optical properties is discussed in [16].

In the presence of a hole collapse $C_r < 1$ (assuming the same value of a drawdown ratio D_{d}), two major changes in the fiber geometry happen. First, while the outside fiber radius is fixed $R_{\mathrm{o}}^{\mathrm{ft}}$, the fiber core radius is reduced $R_i^{\mathrm{f}} = R_i^{\mathrm{ft}} C_r$. Second, the thicknesses of the reflector layers become nonuniform, increasing toward the fiber core, while, on average, layer thicknesses increase as $\bar{d}_{\mathrm{h,l}} \sim d_{\mathrm{h,l}}^t/C_r$. These geometrical changes can significantly modify fiber-transmission spectra.

Thus, as the center wavelength λ_c of a photonic bandgap is proportional to the average reflector layer thickness, then, in the presence of a hole collapse, the center of a bandgap is expected to shift to the longer wavelengths $\lambda_c \sim \lambda_c^t/C_r$ (Fig. 10). We find, however, that in the presence of a hole collapse, the ratio of a bandgap to a midgap (relative bandgap) stays almost unaffected. Another prominent effect of a hole collapse is on the core mode radiation losses. From [27], radiation losses of the bandgap guided core modes scale as $(\lambda_c)^{p-1}/(R_i^{\mathrm{f}})^p$, where exponent p equals 3 for the TE_{0n} modes, while for the HE, EH, and TM modes, exponent p is in the range 1–3, depending strongly on the fiber core size. Thus, in the presence of a hole collapse due to the reduction of the core radius and due to a shift in the center of a bandgap, we expect core mode radiation loss to increase as Loss $\sim C_r^{-(2p-1)}$, which for TE_{01} mode gives Loss $\sim C_r^{-5}$. From more detailed simulations we find that for TE_{01} mode, actual scaling exponent varies from -5 when $C_r \simeq 1$ to almost -7 when $C_r \simeq 0.5$ signifying additional degradation of modal confinement due to nonuniformity in the reflector layer thicknesses.

From the analysis above, it follows that hole collapse mainly leads to the linear shift in the bandgap frequency and a superlinear increase in the radiation losses of the core guided modes.

X. Conclusion

Drawing of multilayer hollow polymer fibers is studied using the thin-filament approximation. The Newtonian, generalized Newtonian, and viscoelastic models of polymer flow are considered. We have numerically characterized the surface tension mitigated hole collapse and the closely related layer thickness nonuniformity. We have demonstrated that by varying various control parameters such as furnace temperature, feeding speed, and pressurization, it is possible to reduce the hole collapse. While the hole pressurization provides a very effective way of compensating for the hollow core collapse, it is found that the final fiber dimensions are very sensitive to the value of the overpressure. Moreover, the draw process can never reach a steady state if the overpressure is larger than a certain critical value. Under the same draw conditions, the hole collapse is more pronounced when non-Newtonian and viscoelastic effects are taken into account. Finally, the hole collapse is identified as a key parameter effecting transmission properties of the resultant hollow Bragg fiber.

References

[1] T. Katsuyama and H. Matsumura, *Infrared Optical Fibers*. Bristol, U.K.: Adam Hilger, 1989.

[2] M. Saito and K. Kikuchi, "Infrared optical fiber sensors," *Opt. Rev.*, vol. 4, no. 5, pp. 527–538, Sep./Oct. 1997.

[3] J. Sanghera and I. Aggarwal, *Infrared Fiber Optics*. Boca Raton, FL: CRC, 1998.

[4] M. Skorobogatiy, "Efficient anti-guiding of TE and TM polarizations in low index core waveguides without the need of omnidirectional reflector," *Opt. Lett.*, vol. 30, no. 22, p. 2991, Nov. 2005.

[5] J. A. Harrington, "A review of IR transmitting, hollow waveguides," *Fiber Integr. Opt.*, vol. 19, no. 3, p. 211, Jul. 2000.

[6] Y. W. Shi, K. Ito, Y. Matsuura, and M. Miyagi, "Multiwavelength laser light transmission of hollow optical fiber from the visible to the mid-infrared," *Opt. Lett.*, vol. 30, no. 21, pp. 2867–2869, Nov. 2005.

[7] B. Temelkuran, S. D. Hart, G. Benoit, J. D. Joannopoulos, and Y. Fink, "Hollow photonic bandgap fibers for NIR applications," *Nature*, vol. 420, no. 6916, pp. 650–653, 2002.

[8] Y. Gao, N. Guo, B. Gauvreau, M. Rajabian, O. Skorobogata, E. Pone, O. Zabeida, L. Martinu, C. Dubois, and M. Skorobogatiy, "Consecutive solvent evaporation and co-rolling techniques for polymer multilayer hollow fiber preform fabrication," *J. Mater. Res.*, vol. 21, no. 9, pp. 2246–2254, 2006.

[9] M. R. Matovich and J. R. A. Pearson, "Spinning a molten threadline—Steady-state isothermal viscous flows," *Ind. Eng. Chem. Fundam.*, vol. 8, no. 3, pp. 512–520, Aug. 1969.

[10] Y. T. Shah and J. R. A. Pearson, "On the stability of nonisothermal fiber spinning," *Ind. Eng. Chem. Fundam.*, vol. 11, no. 2, pp. 145–149, May 1972.

[11] J. A. Burgman, "Liquid glass jets in the forming of continuous fibers," *Glass Technol.*, vol. 11, pp. 110–116, 1970.

[12] F. T. Geyling, "Basic fluid dynamic consideration in the drawing of optical fibers," *Bell Syst. Tech. J.*, vol. 55, no. 8, pp. 1011–1056, 1976.

[13] M. M. Denn, C. J. S. Petrie, and P. Avenas, "Mechanics of steady spinning of a viscoelastic liquid," *AICHE J.*, vol. 21, no. 4, pp. 791–798, 1975.

[14] R. J. Fisher and M. M. Denn, "A theory of isothermal melt spinning and draw resonance," *AICHE J.*, vol. 22, no. 2, pp. 236–245, 1976.

[15] B. D. Freeman, M. M. Denn, R. Keunings, G. E. Molau, and J. Ramos, "Profile development in drawn hollow tubes," *J. Polym. Eng.*, vol. 6, no. 1–4, pp. 171–186, 1986.

[16] E. Pone, C. Dubois, N. Gu, Y. Gao, A. Dupuis, F. Boismenu, S. Lacroix, and M. Skorobogatiy, "Drawing of the hollow all-polymer Bragg fibers," *Opt. Express*, vol. 14, no. 13, p. 5852, Jun. 2006.

[17] A. D. Fitt, K. Furusawa, T. M. Monro, C. P. Please, and D. J. Richardson, "The mathematical modelling of capillary drawing for holey fibre manufacture," *J. Eng. Math.*, vol. 43, no. 2–4, pp. 201–227, Aug. 2002.

[18] S. C. Xue, R. I. Tanner, G. W. Barton, R. Lwin, M. C. J. Large, and L. Poladian, "Fabrication of microstructured optical fibers—Part I: Problem formulation and numerical modeling of transient draw process," *J. Lightw. Technol.*, vol. 23, no. 7, pp. 2245–2254, Jul. 2005.

[19] ——, "Fabrication of microstructured optical fibers—Part II: Numerical modeling of steady-state draw process," *J. Lightw. Technol.*, vol. 23, no. 7, pp. 2255–2266, Jul. 2005.

[20] A. Argyros, M. A. van Eijkelenborg, M. C. J. Large, and I. M. Bassett, "Hollow-core microstructured polymer optical fiber," *Opt. Lett.*, vol. 31, no. 2, pp. 172–174, Jan. 2006.

[21] R. B. Bird, R. C. Amstrong, and O. Hassager, *Dynamics of Polymeric Liquids, Vol. 1, Fluid Mechanics*. New York: Wiley, 1987.

[22] L. J. Cummings and P. D. Howell, "On the evolution of non-axisymmetric viscous fibres with surface tension, inertia and gravity," *J. Fluid Mech.*, vol. 389, no. 1, pp. 361–389, Jun. 1999.

[23] H. A. Barnes and G. P. Roberts, "A simple empirical model describing the steady-state shear and extensional viscosities of polymer melts," *J. Non-Newton. Fluid Mech.*, vol. 44, pp. 113–126, 1992.

[24] H. A. Barnes, J. F. Hutton, and K. Walters, *An Introduction to Rheology*. Amsterdam, The Netherlands: Elsevier, 1989, ch. 2.

[25] S. Wu, "Surface and interfacial tensions of polymer melts. II. Poly(methylmethacrylate), poly(n-butylmethacrylate), and polystyrene," *J. Phys. Chem.*, vol. 74, no. 3, pp. 632–638, Feb. 1970.

[26] R. I. Tanner, *Engineering Rheology*. New York: Oxford Univ. Press, 2000, ch. 9.

[27] S. G. Johnson, M. Ibanescu, M. Skorobogatiy, O. Weisberg, T. D. Engeness, M. Soljačić, S. A. Jacobs, J. D. Joannopoulos, and Y. Fink, "Low-loss asymptotically single-mode propagation in large-core OmniGuide fibers," *Opt. Express*, vol. 9, no. 13, p. 748, Dec. 2001. [Online]. Avaible: http://www.opticsexpress.org/abstract.cfm?URI=OPEX-9-13-748

Elio Pone received the Ph.D. degree in physical engineering from École Polytechnique de Montréal, Montréal, QC, Canada, in 2005.

His current interests include theoretical aspects of fluid dynamics of fiber drawing and component fabrication, as well as design of high-performance electromagnetic phenomena simulators.

Charles Dubois is an associate professor with the Department of Chemical Engineering, École Polytechnique de Montréal, Montréal, QC, Canada. His current interests include polymer synthesis, polymer coating of metals and mineral particles, combustion of powders, and nanocomposits.

Ning Guo is a master program student at the Department of Engineering Physics at École Polytechnique de Montréal, Montréal, QC, Canada, specializing in the preform fabrication and drawing of microstrucured polymer optical fibers.

Suzanne Lacroix is a full professor with the Department of Engineering Physics, École Polytechnique de Montréal, Montréal, QC, Canada. She is a director of the Group Polyphotonique, representing a collective of the researchers in the optics-related areas at École Polytechnique. Her main interests are optical fiber component and subsystem design and fabrication.

Maksim Skorobogatiy received the M.Sc. degree in electrical engineering and computer science and the Ph.D. degree in physics, both from the Massachusetts Institute of Technology (MIT), Cambridge, in 2000 and 2001, respectively.

He then joined MIT start-up OmniGuide Inc., where he worked as a theory and simulations group leader developing hollow Bragg fibers for high-power laser guiding applications. Since 2003, he has been an Associate Professor and a Canada Research Chair in photonic crystals with the Department of Engineering Physics, École Polytechnique de Montréal, Montréal, QC, Canada. His current research activities include polymer photonic crystal and microstructured fiber fabrication and modeling for applications in sensing, telecom, and power transmission.